

A Journal of the Gesellschaft Deutscher Chemiker

# Angewandte Chemie

GDCh

International Edition

[www.angewandte.org](http://www.angewandte.org)

## Accepted Article

**Title:** Relative Local Electron Density Tuning in Metal-Covalent Organic Frameworks for Boosting CO<sub>2</sub> Photoreduction

**Authors:** Mi Zhang, Pei Huang, Jia-Peng Liao, Ming-Yi Yang, Shuai-Bing Zhang, Yu-Fei Liu, Meng Lu, Shun-Li Li, Yue-Peng Cai, and Ya-Qian Lan

This manuscript has been accepted after peer review and appears as an Accepted Article online prior to editing, proofing, and formal publication of the final Version of Record (VoR). The VoR will be published online in Early View as soon as possible and may be different to this Accepted Article as a result of editing. Readers should obtain the VoR from the journal website shown below when it is published to ensure accuracy of information. The authors are responsible for the content of this Accepted Article.

**To be cited as:** *Angew. Chem. Int. Ed.* **2023**, e202311999

**Link to VoR:** <https://doi.org/10.1002/anie.202311999>

## RESEARCH ARTICLE

Relative Local Electron Density Tuning in Metal-Covalent Organic Frameworks for Boosting CO<sub>2</sub> PhotoreductionMi Zhang<sup>\*,[a]</sup>, Pei Huang<sup>\*,[a]</sup>, Jia-Peng Liao<sup>[a]</sup>, Ming-Yi Yang<sup>[a]</sup>, Shuai-Bing Zhang<sup>[a]</sup>, Yu-Fei Liu<sup>[a]</sup>, Meng Lu<sup>\*,[a]</sup>, Shun-Li Li<sup>[a]</sup>, Yue-Peng Cai<sup>[a]</sup> and Ya-Qian Lan<sup>\*,[a]</sup>

[a] Dr. M. Zhang, P. Huang, J.-P. Liao, M.-Y. Yang, S.-B. Zhang, Y.-F. Liu, Dr. M. Lu, Prof. S.-L. Li, Prof. Y.-P. Cai and Prof. Y.-Q. Lan  
 School of Chemistry, South China Normal University, Guangzhou, 510006 (China)  
 E-mail: menglu@m.scnu.edu.cn; yqlan@m.scnu.edu.cn;  
 Homepage: <http://www.yqlangroup.com>

[\*] These authors contributed equally to this work

**Abstract:** The high local electron density and efficient charge carrier separation are two important factors to affect photocatalytic activity, especially for the CO<sub>2</sub> photoreduction reaction. However, the systematic studies on the structure-functional relationship regarding the above two factors based on precisely structure model are rarely reported. Herein, as a proof-of-concept, we developed a new strategy on the evaluation of local electron density by controlling the relative electron-deficient (ED) and electron-rich (ER) intensity of monomer at a molecular level based on three rational-designed vinylene-linked sp<sup>2</sup> carbon-covalent organic frameworks (COFs). As expected, the as-prepared vinylene-linked sp<sup>2</sup> carbon-conjugated metal-covalent organic framework (MCOFs) (VL-MCOF-1) with molecular junction exhibited excellent activities for CO<sub>2</sub>-to-HCOOH conversion (283.41 μmol g<sup>-1</sup> h<sup>-1</sup>) and high selectivity of 97.1%, much higher than the VL-MCOF-2 and g-C<sub>34</sub>N<sub>6</sub>-COF, which is due to the synergistic effect of the multi-electronic metal clusters (Cu<sub>3</sub>(PyCA)<sub>3</sub>) (PyCA = pyrazolate-4-carboxaldehyde) as strong ER roles and cyanopyridine units as ED roles and active sites, as well as the boosted photo-induced charge separation efficiency of vinyl connection and increased light utilization ability. These results not only provide a strategy for regulating the electron-density distribution of photocatalysts at the molecular level but also offers profound insights for metal clusters-based COFs to effective CO<sub>2</sub> conversion.

## Introduction

In the field of photocatalysis, the electron donor-acceptor concept has been widely applied to guide the rational design of efficient catalysts for photocatalytic reactions such as H<sub>2</sub>O splitting, CO<sub>2</sub> reduction, organic photocatalytic reaction, organic solar cells and so on.<sup>[1]</sup> It is well known that the relative electron-deficient (ED) and electron-rich (ER) intensity of units and the rate of charge separation determined the electron density distribution on the molecular level of a junction catalyst, which are also considered to be the essential factors for various catalytic reactions.<sup>[2]</sup> However, the precise regulation of the relative ED and ER intensity of units and the charge separation efficiency are still challenging. Furthermore, the studies on accurate comparison and description the relationship between the ED-ER type molecular junction heterogeneous catalyst and their catalytic activity are still on their early stage.<sup>[3]</sup> Therefore, it is urgent to develop suitable structural models to understand the inherent structure-functional correlation for ED-ER type molecular junction catalysts in depth.

The continuous combustion of fossil fuels all over the world has led to a significant increase in global CO<sub>2</sub> concentration.<sup>[4]</sup> In

recent years, numerous strategies have been developed to address the CO<sub>2</sub> problem. Among them, converting CO<sub>2</sub> into energy fuels by solar energy has been regarded as a promising strategy for achieving the virtuous carbon cycle in nature.<sup>[5]</sup> In this field, the crucial issue to realize practical CO<sub>2</sub> photoreduction is finding highly active photocatalysts. Covalent organic frameworks (COFs) and metal organic frameworks (MOFs) are two widely developed crystalline materials with clear and periodic structures, which not only allow for rational design and customization of their chemical structures, but also easily manipulate them in diverse applications.<sup>[6]</sup> Considering their light-adsorption ability and electronic band structures, many MOFs and COFs are considered as promising CO<sub>2</sub> photoreduction catalysts.<sup>[7]</sup> Especially, MOFs constructed from Ti-O, Zr-O, and Fe-O clusters linked with functional organic linkages have achieved significant progress in the field of photocatalytic CO<sub>2</sub> reduction.<sup>[8]</sup> However, the efficiency and selectivity of CO<sub>2</sub> photoreduction over MOF-based photocatalysts are still rather low, also suffering from low stability.<sup>[7a,9]</sup> Meanwhile, COFs with higher stability and molecular-level precise designability have aroused much attention. Furthermore, due to the diversified linkages and building blocks, the COFs have made many achievements in photocatalytic CO<sub>2</sub> reductions.<sup>[10]</sup> However, the traditional COFs are always constructed by optimizing bulky organic blocks with light elements (such as C, N, O, and H), which are always lacking of multi-electronic storage capability.<sup>[11]</sup> It is a preponderant constraint for COFs acting as effective photocatalysts, given the completion of needful charge transport process to gain all reductive products in CO<sub>2</sub> reduction.<sup>[12]</sup> Metal clusters such as Cu<sub>3</sub>(PyCA)<sub>3</sub> (PyCA = pyrazolate-4-carboxaldehyde) clusters with d<sup>10</sup> metals principally are comprised of low valent metal (including three Cu(I) atoms), which behave ER characters and are able to provide multiple electron when attracted by oxidation-reduction reaction or bias stimulus.<sup>[13]</sup> In addition, most of the reported COFs are usually linked through imine bonds, prevents electronic transmission properties and is a major bottleneck for developing COFs-based photocatalysts with high activity.<sup>[14]</sup> Recently, vinylene-linked COFs with sp<sup>2</sup> carbon-conjugated linkages were developed with featured prominent conductivity and stability, which is a good choice for designing the ED-ER type molecular junction catalysts and helpful for the precise control of local electron density of photocatalysts.<sup>[15]</sup> Consequently, the combination of ER units such as metal clusters and efficient charge transfer channel (denoted as: CTC, vinylene-linkage) into COFs will be an efficacious approach to enhance the activity of photocatalytic CO<sub>2</sub> reduction.

In light of the above discussions, we herein proposed a strategy for realizing the high local electron density of

## RESEARCH ARTICLE

photocatalysts by designing suitable functional groups to regulate the electron-deficient property (EDP) and electron-rich property (ERP) (Figure 1). For the first time, we rational designed and synthesized two new vinylene-linked  $sp^2$  carbon-conjugated metal-covalent organic frameworks (VL-MCOF-1 and VL-MCOF-2) through the Knoevenagel condensation of 3,5-dicyano-2,4,6-trimethylpyridine and 2,4,6-trimethyl-1,3,5-triazine (donated as DCTMP and TMTA, respectively) with  $Cu_3(PyCA)_3$  (Figure 1). In the molecular structure of VL-MCOF-1, the cyano-group in DCTMP not only have stronger EDP but also stronger electron delocation compared to the triazine group of TMTA.<sup>[16]</sup>  $g-C_{34}N_6$ -COF whose structure was similar to VL-MCOF-1 except that the  $Cu_3(PyCA)_3$  was replaced by triazine, was also synthesized to certificate that the  $Cu_3(PyCA)_3$  of VL-MCOFs exhibit potential ERP.<sup>[17]</sup> As results, VL-MCOF-1 features much higher stability, porosity and photosensitivity than  $Cu_3(PyCA)_3$  monomer (Figure S1), higher local electron density than  $g-C_{34}N_6$ -COF and VL-MCOF-2, making it a promising platform for photocatalytic studies. In addition, the VL-MCOF-1 shows well electronic transfer ability due to the conjugated vinylene-linkage, which enhanced the electron transfer from  $Cu_3(PyCA)_3$  to photosensitizer group (DCTMP). As a result, photoactive VL-MCOF-1 has been successfully used as an effective photocatalyst for highly selective  $CO_2$ -to- $HCOOH$  reduction, which showed much superior photocatalytic activities than that of  $g-C_{34}N_6$ -COF, VL-MCOF-2 and individual  $Cu_3(PyCA)_3$ . Furthermore, the density functional theory (DFT) calculations and in-situ fourier transform infrared (FT-IR) studies further revealed that the intrinsic ER  $Cu_3(PyCA)_3$  cluster cooperated with electron withdrawing group (i.e. -CN) in DCTMP together induced with higher local charge distribution on COFs, which caused efficient affinity for  $CO_2$  reduction. This new discovery enables us to comprehend and optimize the local electron density and the rate of charge separation on the photocatalytic performance, thus opening a research pathway for developing improved COFs-based photocatalysts with metal clusters in various applications.

## Results and Discussion

VL-MCOF-1 and VL-MCOF-2 were firstly prepared by the condensation of  $Cu_3(PyCA)_3$  (Figure S1) with DCTMP and TMTA, respectively, which were catalyzed by piperidine under traditional solvothermal conditions (detail see experimental section in supporting information). The powder X-ray diffraction (PXRD) pattern of VL-MCOF-1 displayed principal diffraction peaks at  $6.16^\circ$ ,  $10.60^\circ$ , and  $26.90^\circ$ , assigned to the  $[1, 0, 0]$ ,  $[1, 0, 1]$ , and  $[1, 1, 0]$  crystal facets, respectively (Figure 2a). For VL-MCOF-2, peaks at  $6.29^\circ$ ,  $10.62^\circ$ , and  $27.02^\circ$ , correspond to the  $[1, 0, 0]$ ,  $[2, -1, 0]$ , and  $[0, 0, 1]$  crystal facets, respectively (Figure 2b). Two models were built for the structure of VL-MCOF-1 and VL-MCOF-2 on the basis of the eclipsed (AA) and staggered (AB) stacking conformations, and then geometric and energy optimization was performed through Pawley refinement (detail see structural modeling section in supporting information).

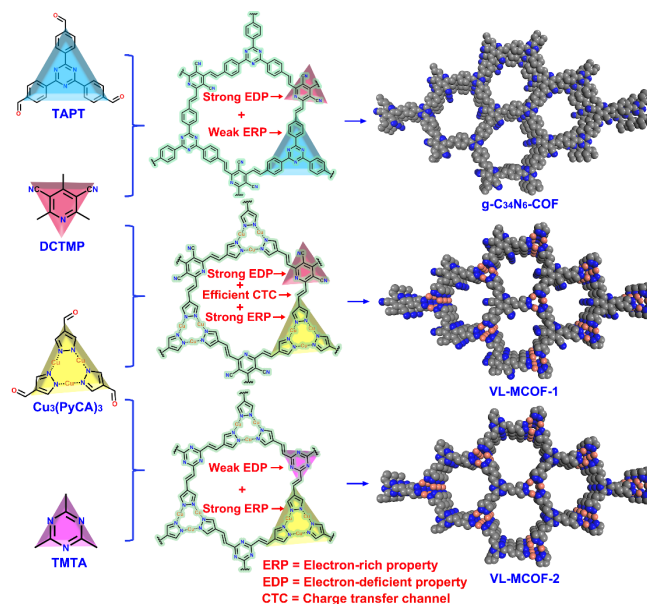


**Figure 1.** Schematic of the synthesis and structure of  $g-C_{34}N_6$ -COF, VL-MCOF-1 and VL-MCOF-2 through Knoevenagel condensation.

The experimental PXRD pattern showed better consistency with the simulated pattern of the eclipsed AA stacking model, as verified by the compared PXRD patterns with an agreement difference ( $R_{wp} = 1.23\%$ ,  $R_p = 10.13\%$  for VL-MCOF-1 and  $R_{wp} = 3.63\%$ ,  $R_p = 2.85\%$  for VL-MCOF-2, respectively). The detailed crystal structure information, including the unit cell parameters, are listed in Table S1 and S2. The simulated structure displayed that the layer spacing of VL-MCOF-1 and VL-MCOF-2 were 3.458 Å and 3.527 Å, respectively (Figure S2). The porosities of VL-MCOFs were estimated with nitrogen adsorption-desorption experiments at 77 K and showed type I reversible isotherms, unveiling microporous characteristics of them. The Brunauer-Emmett-Teller (BET) surface areas of VL-MCOF-1 and VL-MCOF-2 were determined to be 541.31 and 452.23  $m^2 g^{-1}$ , respectively, (Figure S3). The measured pore sizes ( $\sim 1.38$  and 1.42 nm) for VL-MCOF-1 and VL-MCOF-2 were in accordance with the theoretical values (Figures S2 and S4).

The chemical constitution of obtained VL-MCOFs was further analyzed using Fourier transform infrared (FT-IR) and  $^{13}C$  cross-polarization/magic angle spinning solid-state nuclear magnetic resonance (CP/MAS ssNMR) spectroscopy. In FT-IR spectra (Figure 2c), the emerging signals of these VL-MCOFs-1 at about 1625 and 970  $cm^{-1}$  were belonged to trans-C=C linkages and the intense peak at 2225  $cm^{-1}$  was attributed to the cyano group.<sup>[18]</sup> As shown in Figure S5, the peaks at 1628 and 974  $cm^{-1}$  belonging to trans-C=C bonds appeared in VL-MCOF-2 (red curve), which also confirmed the successful condensation reaction between and TMTA and  $Cu_3(PyCA)_3$ . In these VL-MCOFs, no C=O stretching vibrations could be detected, which manifested a high degree of polymerization. In  $^{13}C$  CP/MAS ssNMR spectra of VL-MCOF-1 (Figure S6), the signal at  $\sim 116$  ppm was attributed to cyano groups and peak at  $\sim 132$  ppm was corresponded to the olefin carbons (C=C).<sup>[19]</sup> The strong resonance at 99 ppm originated from the pyrazole carbon. As for VL-MCOF-2 (Figure S7), The signal at  $\sim 174$  ppm was attributed to the C of the triazine ring.<sup>[20]</sup> The peaks at 131 ppm could be assigned to vinylene (C=C) carbons, while a clear peak at 118 ppm was belonged to pyrazole carbon. All the above results substantially verified the structural integrity of the VL-MCOFs.

## RESEARCH ARTICLE

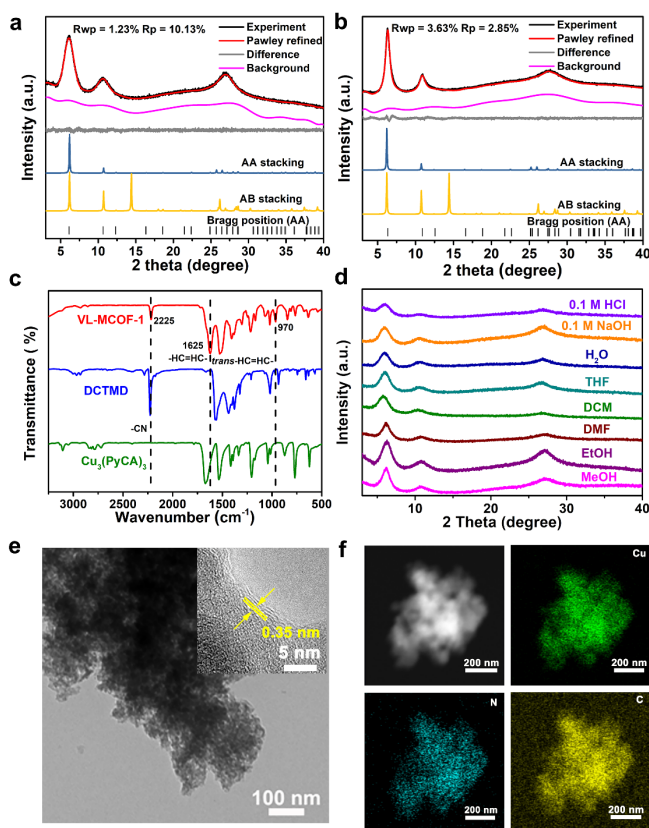


**Figure 2.** Experimental, Pawley refined and simulated PXRD patterns (AA stacking and AB stacking mode) of (a) VL-MCOF-1 and (b) VL-MCOF-2. (c) FT-IR spectra of VL-MCOF-1. (d) Chemical stability of VL-MCOF-1. (e) TEM image of VL-MCOF-1. Inset: HRTEM image and lattice fringes of VL-MCOF-1. (f) Element mapping of VL-MCOF-1.

The thermostabilities of VL-MCOFs were validated through thermogravimetric analysis (TGA, Figures S8-S11). At the first stage, the VL-MCOF started with de-solvation at low temperatures (<120 °C) under N<sub>2</sub> atmosphere (Figures S8-S9). After that, the weight of VL-MCOF showed gradually decrease without an obvious platform and then sharply diminished at ~350 °C, which was attributed to the collapse of Cu<sub>3</sub>(PyCA)<sub>3</sub> units, as the framework began to degrade. Furthermore, the degradation in the range of 400-500 °C was attributed to the crack of aromatic organic linkers (DCTMP, TMTA, and HPyCA). Besides, under O<sub>2</sub> atmosphere (Figures S10-S11), the VL-MCOF could only stable up to ~240 °C (with thermal decomposition temperatures of 238 °C and 241 °C for VL-MCOF-1 and VL-MCOF-2, respectively) and then rapidly transformed into cupric oxide. The chemical stability of VL-MCOFs was examined through soaking them into various solvents (including menthol (MeOH), ethanol (EtOH), N, N-dimethylformamide (DMF), dichloromethane (DCM), tetrahydrofuran (THF), water and acid/base such as 0.1 M HCl, and 0.1 M NaOH at room temperature for at least 24 h. No obvious changes were found in the PXRD of the VL-MCOFs after the treatment (Figure 2d and Figure S12), indicating their structural robustness.

The morphologies of the obtained COFs were further characterized using transmission electron microscopy (TEM) and scanning electron microscopy (SEM). As for VL-MCOFs, the SEM and TEM tests showed rough spherical morphologies (domain sizes in the range of >50 nm) (Figures 2e and S13-S14). In addition, directional lattice fringes could be found in high

resolution TEM (HR-TEM) image and a lattice spacing of 0.35 nm was ascribed to the layer pattern (001 plane) of VL-MCOF-1, the appearance of lattice fringe verifying the high crystallinity of VL-MCOF-1 (inset of Figure 2e). Moreover, the energy-dispersive X-ray element mapping of VL-MCOF-1 showed that C, N, and Cu were evenly distributed over the nanoparticles, indicating the high element-uniformity in the COF (Figure 2f). X-ray photoelectron spectroscopy (XPS) measurements were also conducted on these COFs to unveil their chemical composition and valence state. As shown in Figures S15-S18, a series of peaks assigned to C, N, O and Cu in the survey spectra indicated the presence of above elements on VL-MCOFs. In the high-resolution C 1s spectrum of VL-MCOFs (Figures S16 and S18), the binding energy peaks at about 284.1, 284.8, 285.7, 286.9 and 288.2 eV correspond to C=C, C-C, C=N in pyridine, C≡N and C=N in pyrazole ring for VL-MCOF-1, and the binding energy peaks at about 284.0, 284.8, 285.9, and 288.3 eV correspond to C=C, C-C, C=N in triazine, and C=N in pyrazole ring for VL-MCOF-2. In addition, The high-resolution N 1s spectra were deconvoluted into three peaks at 398.6, 399.8 and 400.6 eV revealing the existence of C≡N, pyrazole N and pyridine N for VL-MCOF-1, and two peaks at 398.7 and 400.1 eV revealed the existence of triazine N and pyrazole N for VL-MCOF-2. The high-resolution O 1s spectrum of both samples could be deconvoluted into one Gaussian peaks associated with H-O of H<sub>2</sub>O respectively. The Cu 2p spectra (Figures S16 and S18) of VL-MCOFs showed two dominant peaks of Cu 2p<sub>1/2</sub> and Cu 2p<sub>3/2</sub> as well as corresponding satellite peaks of them. The Cu 2p<sub>1/2</sub> region exhibited two deconvoluted peaks at approximately 955.00 and 952.9 eV, corresponding to Cu<sup>2+</sup> and Cu<sup>1+</sup>, respectively. Likewise, the Cu 2p<sub>3/2</sub> region provided Cu<sup>2+</sup> at about 935.08 eV and Cu<sup>1+</sup> at 933.06 eV for VL-MCOF-1.<sup>[21]</sup> As for g-C<sub>34</sub>N<sub>6</sub>-COF whose structure was similar to VL-MCOF-1 except that the Cu<sub>3</sub>(PyCA)<sub>3</sub> core was replaced by triazine, was also synthesized to certificate that the Cu<sub>3</sub>(PyCA)<sub>3</sub> core of VL-MCOFs could act as potential ER units. The structure and morphology of g-C<sub>34</sub>N<sub>6</sub>-COF were also well characterized by PXRD, TGA, FI-IR, SEM and TEM tests (Figures S19-S24).

The photocurrent response was then conducted to character the separating efficiency of carriers produced by photo. The light-current response intensity of VL-MCOF-1 was obviously stronger than that of VL-MCOF-2, g-C<sub>34</sub>N<sub>6</sub>-COF, and Cu<sub>3</sub>(PyCA)<sub>3</sub>, which indicated the VL-MCOF-1 had higher electron migration efficiency and would donate more available surface carriers in photocatalytic process, saw from Figure 3a. Electrochemical impedance spectroscopy (EIS) is an effective approach for evaluating the kinetic characteristics of electrons and holes. In Figure 3b, VL-MCOF-1 with smaller electronic transmission resistance indicated that it possessed speedier interface charge transport rate than others. UV-Vis diffuse reflectance spectroscopy (DRS) was also used for detecting the optical properties of these samples (Figure 3c), and then we discovered that the VL-MCOF-1 exhibited stronger photo absorption capability (from ultraviolet to visible light region) compared to other contrastive samples. The optical band gaps were also analyzed and determined in view of Tauc plot analysis, which gave rise to 1.93, 2.07, 2.37, and 2.31 eV for VL-MCOF-1, VL-MCOF-2, g-C<sub>34</sub>N<sub>6</sub>-COF and Cu<sub>3</sub>(PyCA)<sub>3</sub>, respectively (Figure 3d).<sup>[22]</sup> Furthermore, Mott-Schottky (MS) measurements were conducted to determine the conduction-band (CB) positions of these samples, allowing for rough inference of possible reduction

## RESEARCH ARTICLE

products (Figures S25-S28). The CB positions of VL-MCOF-1, VL-MCOF-2, g-C<sub>34</sub>N<sub>6</sub>-COF, and Cu<sub>3</sub>(PyCA)<sub>3</sub> were -0.69, -0.77, -0.62 and -0.66 eV, which were more negative than the reduction potentials of loads of photocatalytic yields such as HCOOH (0.61 eV vs. NHE), CO (0.53 eV vs. NHE), etc., suggesting that the photogenerated charges could transfer to the CO<sub>2</sub> for the reduction process. By combining the band gaps of these samples from UV-Vis absorption data and CB positions of them from MS data, it could be determined that their valence band (VB) positions are 1.24, 1.30, 1.75, and 1.65 eV, respectively (Figure 3e). Volumetric CO<sub>2</sub> adsorption measurements were conducted on activated samples at 298 K, and the CO<sub>2</sub> uptakes of the VL-MCOF-1, VL-MCOF-2, g-C<sub>34</sub>N<sub>6</sub>-COF, and Cu<sub>3</sub>(PyCA)<sub>3</sub> were determined to be 33.21, 32.08, 20.64 and 2.75 cm<sup>3</sup> g<sup>-1</sup> in Figure 3f. Because the cluster (Cu<sub>3</sub>(PyCA)<sub>3</sub>) and the cyano of the crystalline porous framework (VL-MCOF-1) were considered as ideal sites that could adsorb CO<sub>2</sub>, VL-MCOF-1 possessed relatively higher adsorption capacities than VL-MCOF-2, g-C<sub>34</sub>N<sub>6</sub>-COF and Cu<sub>3</sub>(PyCA)<sub>3</sub>.

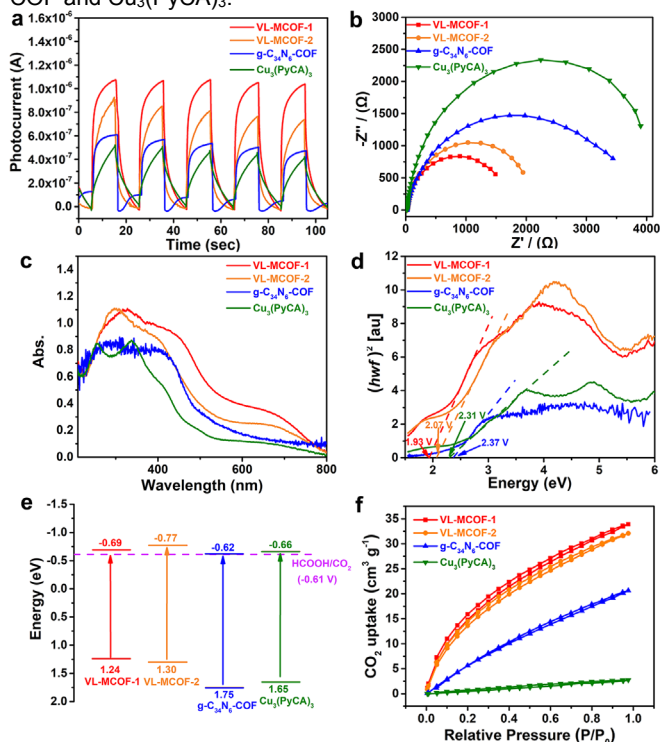


**Figure 3.** (a) Transient photocurrent response, (b) EIS Nyquist plots and, (c) Solid-state UV-Vis absorption spectra, (d) Tauc plots, (e) Band-structure diagram, (f) CO<sub>2</sub> adsorption-desorption isotherm of VL-MCOF-1, VL-MCOF-2, g-C<sub>34</sub>N<sub>6</sub>-COF and Cu<sub>3</sub>(PyCA)<sub>3</sub>.

The photic driving CO<sub>2</sub> reduction of VL-MCOF-1, VL-MCOF-2, g-C<sub>34</sub>N<sub>6</sub>-COF, and Cu<sub>3</sub>(PyCA)<sub>3</sub> were conducted under a pure CO<sub>2</sub> atmosphere in water using triisopropanolamine (TIPA) as the electron donor, without any photosensitizer and noble-metal cocatalyst. From Figures 4a and 4b, it can be seen that the HCOOH yield of these samples continues to increase with the prolongation of reaction time. After 8 hours, the HCOOH production of VL-MCOF-1 achieved about 283.41 μmol g<sup>-1</sup> h<sup>-1</sup>, higher than VL-MCOF-2 (about 195.57 μmol g<sup>-1</sup> h<sup>-1</sup>), almost 9 times higher than that of g-C<sub>34</sub>N<sub>6</sub>-COF (about 31.53 μmol g<sup>-1</sup> h<sup>-1</sup>) and 15 times higher than that of Cu<sub>3</sub>(PyCA)<sub>3</sub> (about 18.80 μmol g<sup>-1</sup> h<sup>-1</sup>). The catalytic results showed that HCOOH was the solely liquid product, while slightly competitive H<sub>2</sub> and CO were detected. Based on the yield distribution (Figure 4b), the photocatalytic

selectivity of CO<sub>2</sub>-to-HCOO<sup>-</sup> conversion for VL-MCOF-1, VL-MCOF-2, g-C<sub>34</sub>N<sub>6</sub>-COF and Cu<sub>3</sub>(PyCA)<sub>3</sub> were determined to be 97.13%, 96.34%, 82.09% and 81.39% respectively. To confirm the photocatalytic activity of VL-MCOF, a series of deletional control experiments were conducted including in the absence of photocatalysts or sacrificial agent, and no detectable products were observed in the reaction system (see Figure S29). We assumed that the higher photocatalytic activity of VL-MCOF-1 was attribute to the effective combination of strong ER Cu<sub>3</sub>(PyCA)<sub>3</sub> and strong ED DCTMP, the enhanced photo absorption as well as the fast separation of photoinduced holes and electrons. In addition, such special VL-MCOF-1 displayed excellent stability in long-term photocatalysis. It could be seen that the photocatalyst still kept a good catalytic efficiency without a significant downward trend after four cycles from Figure 4c, suggesting good durability of VL-MCOF-1. The long single reaction circle test showed that the rate of HCOOH formation showed no obviously decrease with irradiation time before 28 h, after that the formation rate began to largely decreased due to the consume of sacrificial agents or the photocorrosion effect of COFs (Figure S30). To explore the possibility of other metal such as Ag clusters as ER, we also synthesized a same type MCOF structure based on Ag<sub>3</sub>L<sub>3</sub> (named Ag<sub>3</sub>L<sub>3</sub>-MCOF, L = 4-(3,5-dimethyl-1H-pyrazol-4-yl) benzaldehyde). The structure, characterization and performance test results were shown in Figure S31. The Ag<sub>3</sub>L<sub>3</sub>-MCOF for CO<sub>2</sub> photoreduction to HCOOH was then studied, and the results showed the HCOOH yield of it is 94.2 μmol g<sup>-1</sup> h<sup>-1</sup>, which behaved much lower activity than VL-MCOF-1. More importantly, no evident changes were observed in the PXRD pattern, TEM, and SEM images after the photocatalytic process, confirming the superb long-term durability of VL-MCOFs (Figures S32-S37).

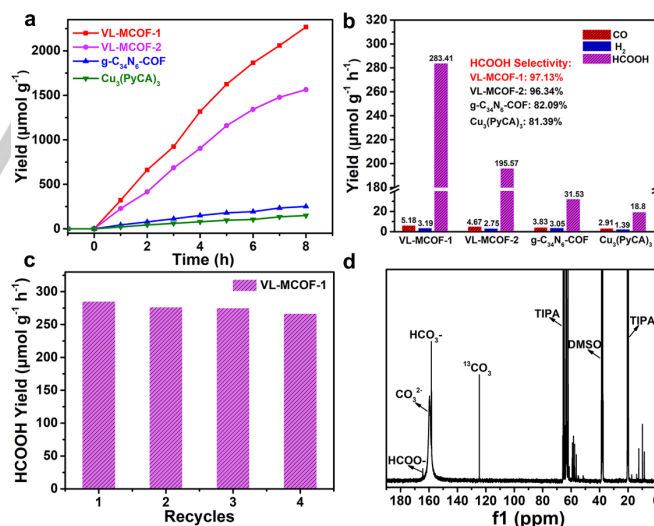


**Figure 4.** (a) The relationship between the yield of HCOOH and the irradiation time, and (b) The selectivity of HCOOH and the yield distribution of different photoreduction products for VL-MCOF-1, VL-MCOF-2, g-C<sub>34</sub>N<sub>6</sub>-COF and Cu<sub>3</sub>(PyCA)<sub>3</sub>. (c) Durability measurements of VL-MCOF-1 (8 h test per cycle). (d) The <sup>13</sup>C NMR spectrum of the product was obtained by adding <sup>13</sup>CO<sub>2</sub> into the reaction of VL-MCOF-1.

In addition, to further verify the photocatalytic activities for VL-MCOF-1, an isotopic <sup>13</sup>CO<sub>2</sub> experiment under the same photocatalysis conditions was conducted to determine the C source origin of the generated HCOO<sup>-</sup>, and the yields were further confirmed through <sup>13</sup>C NMR spectroscopy. As illustrated in

## RESEARCH ARTICLE

Figures 4d and S38, the  $^{13}\text{C}$  NMR spectrum provided an obvious signal at 164.5 ppm, corresponding to  $\text{HCOO}^-$ .<sup>[23]</sup> In addition, these signals vanished when using  $^{12}\text{CO}_2$  to replace  $^{13}\text{CO}_2$ , apart from the extra peaks of DMSO and TIPA. The above fact clearly proves that the generated  $\text{HCOO}^-$  indeed comes from  $\text{CO}_2$ . Therefore, it can be concluded that VL-MCOF-1 is a real active catalyst for converting  $\text{CO}_2$  to  $\text{HCOO}^-$  with irradiation. The liquid product in the reaction system was then checked by  $^1\text{H}$  NMR (Figure S39). The results showed that except  $\text{HCOO}^-$ , no other liquid product was detected.

The in-situ FT-IR analysis of VL-MCOF-1 for photocatalytic  $\text{CO}_2$  reduction was then conducted to study the photocatalytic mechanism. In Figure 5a, there were five peaks at 1643, 1549, 1424, 1329, and 1265  $\text{cm}^{-1}$  respectively, attributed to the C=O, asymmetric, symmetric, C-O stretch, OH deformation of  $\text{HCOOH}^*$ , which suggested the key intermediate of  $\text{CO}_2$  photoreduction to  $\text{HCOOH}$ .<sup>[24]</sup> The band centered at 1533  $\text{cm}^{-1}$  was attributed to asymmetric stretch of O-C-O, indicating the formation of  $\text{OCHO}^*$  on VL-MCOF-1 during the processing of  $\text{CO}_2$  reduction.<sup>[25]</sup> In order to understand the photo-excitation process and catalytic reaction mechanisms, the DFT calculations were applied. The electronic transitions for these two COFs was shown in Figure 5b, c. The first excitation contribution, that was, from highest occupied molecular orbital (HOMO) to lowest unoccupied molecular orbital (LUMO) models showed that the ER  $\text{Cu}_3(\text{PyCA})_3$  fragment dominated the HOMO while the LUMO was mainly contributed by the DCTMP and TMTA part for VL-MCOF-1 and VL-MCOF-2, respectively. These results confirmed that the  $\text{Cu}_3(\text{PyCA})_3$  played the ER role, consistent with the proposed charge transfer mechanism. Furthermore, we could also conclude that the electron withdrawing group (i.e. -CN) in DCTMP induced with higher local charge distribution on COFs, which caused efficient affinity for  $\text{CO}_2$  reduction.<sup>[26]</sup> To ascertain the active sites of  $\text{CO}_2$  reduction at the molecular level, the Gibbs free energy was then calculated for  $\text{CO}_2$  reduction processes on these COFs. We calculated the possible active sites for  $\text{CO}_2$  reduction, including -CN, -C=C, and N of pyridine for VL-MCOF-1 and -N3 (three identical N atoms on triazine) and -C=C for VL-MCOF-2 (Figure 5d and S41). Interestingly, we found that the -CN sites would spontaneously receive electrons and protons after the  $\text{CO}_2$  adsorption and activation process, thus efficiently transforming  $\text{CO}_2$  into  $\text{HCOOH}$ . The proton-coupled electron transfer step to generate  $\text{OCHO}^*$  from the adsorbed  $\text{CO}_2$  acted as the key role to determine which path would proceed.<sup>[27]</sup> In detail, the free energy change of  $\text{CO}_2$  into  $\text{OCHO}^*$  was -0.862 eV and 0.540 eV for -CN and -C=C site, respectively. It was noted that the N of pyridine on VL-MCOF-1 was also considered as the possible active site for  $\text{CO}_2$  reduction. However, the results showed that  $^*\text{OCHO}$  could not be stably adsorbed on N, which hindered the further reaction. We also calculated the free energy changes and comparisons including three  $\text{CO}_2$  reduction pathways ( $\text{CO}_2\text{-OCHO}^*\text{-HCOOH}$  pathway,  $\text{CO}_2\text{-COOH}^*\text{-HCOOH}$  pathway and  $\text{CO}_2\text{-COOH}^*\text{-CO}$  pathway) and side reaction pathway (hydrogen evolution reaction (HER) with  $\text{H}^*$  intermediates) at the VL-MCOF-1 (Figure S42). As could be seen from Figure S42, the rate-determining step (either  $\text{CO}_2\text{-OCHO}^*\text{-HCOOH}$  or  $\text{CO}_2\text{-COOH}^*\text{-HCOOH}$  pathway) was the generate of  $\text{CO}_2^*$  (0.686 eV), while the dGmax of photocatalytic  $\text{CO}_2$  reduction to CO was 1.613 eV (Figure S42c) and HER to  $\text{H}_2$  is 1.051 eV (Figure S42d), which was much large than  $\text{CO}_2$ -to- $\text{HCOOH}$ . According to the selectivity relationship, the smaller the dGmax, the higher the selectivity. This indicated the

photocatalytic  $\text{CO}_2$  reduction to format had the highest selectivity, which was consistent with the experiments. Furthermore, for the two competitive reaction pathways of  $\text{CO}_2$ -to- $\text{HCOOH}$ , the free energy calculation results showed that the  $\text{OCHO}^*$  transformed into  $\text{HCOOH}^*$  intermediate was exothermic with free energy change of -0.340 eV (blue dashed box in Figure S40a). However, the  $\text{COOH}^*$  transformed into  $\text{HCOOH}^*$  intermediate was endothermic with free energy change of +0.315 eV (blue dashed box in Figure S40b). Therefore, compared with  $\text{CO}_2\text{-COOH}^*\text{-HCOOH}$ , the  $\text{CO}_2\text{-OCHO}^*\text{-HCOOH}$  pathway showed better activity. For VL-MCOF-2, no spontaneous process was observed, which might be due to the relatively weak electron density on the LUMO site. Despite this, the free energy change of  $\text{CO}_2$  into  $\text{OCHO}^*$  on VL-MCOF-2 was 1.471 eV and 0.514 eV for -N3 and -C=C sites, respectively. These results suggested the most probable active sites for  $\text{CO}_2$  reduction on VL-MCOF-2 was -C=C units. To further elucidate the electron-transport direction of  $\text{Cu}_3(\text{PyCA})_3$  and DCTMP through experiments, high-resolution in-situ XPS measurements were also performed on the Cu 2p state of VL-MCOF-1 (Figure S40). The positive shift in the Cu 2p binding energy with light excitation was owing to the electron-density reduction at the Cu sites. The above results exhibited that the direction of photogenerated electrons transfer was from  $\text{Cu}_3(\text{PyCA})_3$  to DCTMP, consistent with the theoretical results. Above all, the in-situ FTIR, in-situ XPS, and DFT calculations synergistically confirmed the  $\text{CO}_2$ -to- $\text{HCOOH}$  catalytic process: Under the photo-excitation, the electron was transferred from  $\text{Cu}_3(\text{PyCA})_3$  (ER unit) to -CN or triazine group (ED unit) in VL-MCOF-1 then the adsorbed  $\text{CO}_2$  in -CN sites was activated and underwent proton-coupled electron transport step to produce  $\text{OCHO}^*$  then transformed to  $\text{HCOOH}$ .<sup>[28]</sup> In this process, the stronger EDP and ERP will cause the higher local electron density in active sites, which is beneficial to the electron transfer and utilization, finally improving the efficiency of photocatalytic  $\text{CO}_2$  reduction (Figure 5e).

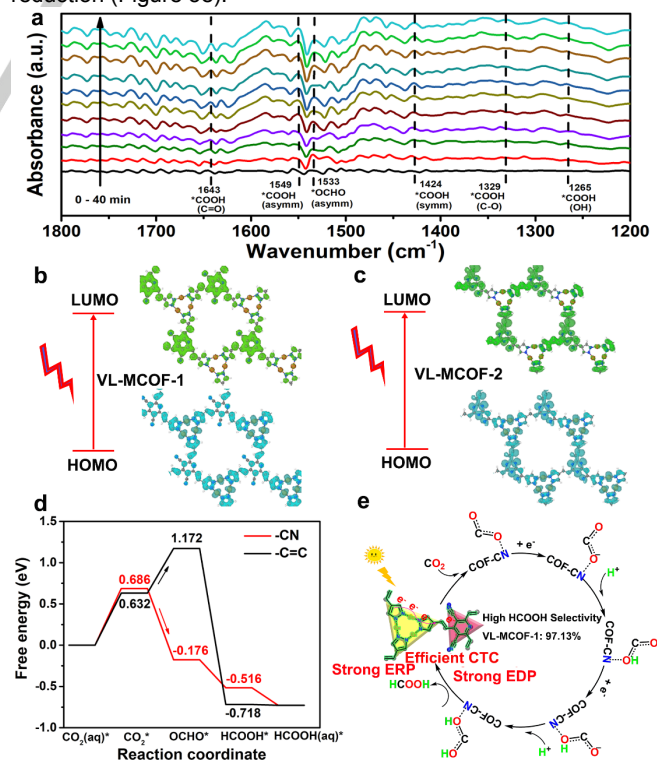


**Figure 5.** (a) In-situ FT-IR spectra for photocatalytic  $\text{CO}_2$  reduction on VL-MCOF-1. The LUMO and HOMO orbitals calculated for (b) VL-MCOF-1 and (c)

## RESEARCH ARTICLE

VL-MCOF-2. (d) Free energy diagram (FED) of VL-MCOF-1. (e) Plausible mechanism for photocatalytic CO<sub>2</sub> reduction over VL-MCOF-1 under light irradiation.

## Conclusion

In conclusion, we synthesized a series of sp<sup>2</sup> carbon-crystalline frameworks based on the Knoevenagel condensation as photocatalysts for CO<sub>2</sub> reduction reaction via systematic engineering of building blocks as structural models to regulate the local electron density and accelerate the rate of charge separation. In light of this, the well-designed VL-MCOF-1 as photocatalyst showed excellent activity for CO<sub>2</sub> reduction to HCOOH with 283.41 μmol g<sup>-1</sup> h<sup>-1</sup> and superior selectivity (> 97%), better than VL-MCOF-1, g-C<sub>34</sub>N<sub>6</sub>-COFs, Cu<sub>3</sub>(PyCA)<sub>3</sub> and most of crystalline framework catalysts. The experimental and theoretical studies verified that the Cu<sub>3</sub>(PyCA)<sub>3</sub> acted as the strong ERP role, and the organic chromophore with cyano group played the role of active site for photocatalytic CO<sub>2</sub>-to-HCOOH transform with strong EDP, thus contributing high photocatalytic activity. This work demonstrates the potential to regulate local charge distributions by fine-tuning the EDP and ERP, which can shed new light on the rational design of efficient crystalline photocatalysts with metal clusters.

## Acknowledgements

This work was supported by the NSFC (Nos. 22225109, 22071109, 22105080, and 22201083), the Project funded by the China Postdoctoral Science Foundation (Nos. 2020M682748 and 2021M701270), the Guangdong Basic and Applied Basic Research Foundation (Grant 2023A1515010779 and 2023A1515010928), the Guangzhou Basic and Applied Basic Research Fund Project (Grant 202102020209), China National Postdoctoral Program for Innovative Talents (BX20220115).

**Keywords:** Metal-covalent organic frameworks • Vinyl linkages • Molecular junction • Electron-density distribution • Photocatalytic CO<sub>2</sub> reduction

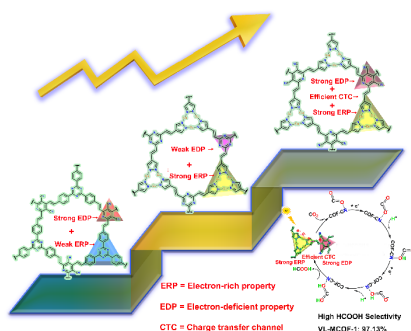
- [1] a) Z. Li, T. Deng, S. Ma, Z. Zhang, G. Wu, J. Wang, Q. Li, H. Xia, S.-W. Yang, X. Liu, *J. Am. Chem. Soc.* **2023**, *145*, 8364-8374; b) J. Yang, S. Ghosh, J. Roeser, A. Acharya, C. Pensche, Y. Tsutsui, J. Rabeah, T. Wang, S. Y. Djoko Tameu, M.-Y. Ye, J. Grüneberg, S. Li, C. Li, R. Schomäcker, R. Van De Krol, S. Seki, P. Saalfrank, A. Thomas, *Nat. Commun.* **2022**, *13*, 6317; c) S. Li, L. Li, Y. Li, L. Dai, C. Liu, Y. Liu, J. Li, J. Lv, P. Li, B. Wang, *ACS Catal.* **2020**, *10*, 8717-8726; d) S. Barman, A. Singh, F. A. Rahimi, T. K. Maji, *J. Am. Chem. Soc.* **2021**, *143*, 16284-16292.
- [2] a) Y. Liu, X. Jiang, L. Chen, Y. Cui, Q.-Y. Li, X. Zhao, X. Han, Y.-C. Zheng, X.-J. Wang, *J. Mater. Chem. A* **2023**, *11*, 1208-1215; b) L. Guo, J. Gong, C. Song, Y. Zhao, B. Tan, Q. Zhao, S. Jin, *ACS Energy Lett.* **2020**, *5*, 1300-1306.
- [3] a) J. Zhao, J. Ren, G. Zhang, Z. Zhao, S. Liu, W. Zhang, L. Chen, *Chem. Eur. J.* **2021**, *27*, 10781-10797; b) D. Chen, W. Chen, Y. Wu, L. Wang, X. Wu, H. Xu, L. Chen, *Angew. Chem. Int. Ed.* **2023**, *62*, e202217479.
- [4] a) D. Hong, T. Kawanishi, Y. Tsukakoshi, H. Kotani, T. Ishizuka, T. Kojima, *J. Am. Chem. Soc.* **2019**, *141*, 20309-20317; b) Y. Kuramochi, Y. Fujisawa, A. Satake, *J. Am. Chem. Soc.* **2020**, *142*, 705-709.
- [5] a) T. Ouyang, H.-J. Wang, H.-H. Huang, J.-W. Wang, S. Guo, W.-J. Liu, D.-C. Zhong, T.-B. Lu, *Angew. Chem. Int. Ed.* **2018**, *57*, 16480-16485; b) T. Ouyang, H.-H. Huang, J.-W. Wang, D.-C. Zhong, T.-B. Lu, *Angew. Chem. Int. Ed.* **2017**, *56*, 738-743.
- [6] a) T. He, Z. Zhao, R. Liu, X. Liu, B. Ni, Y. Wei, Y. Wu, W. Yuan, H. Peng, Z. Jiang, Y. Zhao, *J. Am. Chem. Soc.* **2023**, *145*, 6057-6066; b) W. Zhang, L. Chen, S. Dai, C. Zhao, C. Ma, L. Wei, M. Zhu, S. Y. Chong, H. Yang, L. Liu, Y. Bai, M. Yu, Y. Xu, X.-W. Zhu, Q. Zhu, S. An, R. S. Sprick, M. A. Little, X. Wu, S. Jiang, Y. Wu, Y.-B. Zhang, H. Tian, W.-H. Zhu, A. I. Cooper, *Nature* **2022**, *604*, 72-79; c) C. Gropp, T. Ma, N. Hanikel, O. M. Yaghi, *Science* **2020**, *370*, eabd6406; d) K. Sun, O. J. Silveira, Y. Ma, Y. Hasegawa, M. Matsumoto, S. Kera, O. Krejčí, A. S. Foster, S. Kawai, *Nat. Chem.* **2023**, *15*, 136-142.
- [7] a) R. Li, W. Zhang, K. Zhou, *Adv. Mater.* **2018**, *30*, 1705512; b) T. He, Y. Zhao, *Angew. Chem. Int. Ed.* **2023**, *62*, e202303086; c) H. L. Nguyen, *Adv. Energy Mater.* **2020**, *10*, 2002091.
- [8] a) W. Lu, Z. Wei, Z.-Y. Gu, T.-F. Liu, J. Park, J. Park, J. Tian, M. Zhang, Q. Zhang, T. Gentle III, M. Bosch, H.-C. Zhou, *Chem. Soc. Rev.* **2014**, *43*, 5561-5593; b) Y. Fu, D. Sun, Y. Chen, R. Huang, Z. Ding, X. Fu, Z. Li, *Angew. Chem. Int. Ed.* **2012**, *51*, 3364-3367; c) D. Sun, Y. Fu, W. Liu, L. Ye, D. Wang, L. Yang, X. Fu, Z. Li, *Chem. Eur. J.* **2013**, *19*, 14279-14285; d) K. G. M. Laurier, F. Vermoortele, R. Ameloot, D. E. De Vos, J. Hofkens, M. B. J. Roelfaers, *J. Am. Chem. Soc.* **2013**, *135*, 14488-14491.
- [9] a) D. Li, M. Kassymova, X. Cai, S.-Q. Zang, H.-L. Jiang, *Coord. Chem. Rev.* **2020**, *412*, 213262; b) C. A. Trickett, A. Helal, B. A. Al-Maythallony, Z. H. Yamani, K. E. Cordova, O. M. Yaghi, *Nat. Rev. Mater.* **2017**, *2*, 17045.
- [10] a) C. Qian, L. Feng, W. L. Teo, J. Liu, W. Zhou, D. Wang, Y. Zhao, *Nat. Chem. Rev.* **2022**, *6*, 881-898; b) X. Guan, Q. Fang, Y. Yan, S. Qiu, *Acc. Chem. Res.* **2022**, *55*, 1912-1927; c) S. Tao, D. Jiang, *CCS Chemistry* **2021**, *3*, 2003-2024; d) M. Lu, M. Zhang, J. Liu, Y. Chen, J.-P. Liao, M.-Y. Yang, Y.-P. Cai, S.-L. Li, Y.-Q. Lan, *Angew. Chem. Int. Ed.* **2022**, *61*, e202200003.
- [11] C. Xia, K. O. Kirlikovali, T. H. C. Nguyen, X. C. Nguyen, Q. B. Tran, M. K. Duong, M. T. Nguyen Dinh, D. L. T. Nguyen, P. Singh, P. Raizada, V.-H. Nguyen, S. Y. Kim, L. Singh, C. C. Nguyen, M. Shokouhimehr, Q. V. Le, *Coord. Chem. Rev.* **2021**, *446*, 214117.
- [12] a) J. Dong, X. Han, Y. Liu, H. Li, Y. Cui, *Angew. Chem. Int. Ed.* **2020**, *59*, 13722-13733; b) E. Nikoloudakis, I. López-Duarte, G. Charalambidis, K. Ladomenou, M. Ince, A. G. Coutsolelos, *Chem. Soc. Rev.* **2022**, *51*, 6965-7045; c) Y.-R. Wang, Q. Huang, C.-T. He, Y. Chen, J. Liu, F.-C. Shen, Y.-Q. Lan, *Nat. Commun.* **2018**, *9*, 4466.
- [13] a) R.-J. Wei, H.-G. Zhou, Z.-Y. Zhang, G.-H. Ning, D. Li, *CCS Chemistry* **2021**, *3*, 2045-2053; b) H.-G. Zhou, R.-Q. Xia, J. Zheng, D. Yuan, G.-H. Ning, D. Li, *Chem. Sci.* **2021**, *12*, 6280-6286.
- [14] a) K. Geng, T. He, R. Liu, S. Dalapati, K. T. Tan, Z. Li, S. Tao, Y. Gong, Q. Jiang, D. Jiang, *Chem. Rev.* **2020**, *120*, 8814-8933; b) H. Yang, M. Hao, Y. Xie, X. Liu, Y. Liu, Z. Chen, X. Wang, G. I. N. Waterhouse, S. Ma, *Angew. Chem. Int. Ed.* **2023**, *62*, e202303129.
- [15] a) S. Xu, H. Sun, M. Addicoat, B. P. Biswal, F. He, S. Park, S. Paasch, T. Zhang, W. Sheng, E. Brunner, Y. Hou, M. Richter, X. Feng, *Adv. Mater.* **2021**, *33*, 2006274; b) Y. Liu, W. Zhou, W. L. Teo, K. Wang, L. Zhang, Y. Zeng, Y. Zhao, *Chem* **2020**, *6*, 3172-3202.
- [16] C. Mo, M. Yang, F. Sun, J. Jian, L. Zhong, Z. Fang, J. Feng, D. Yu, *Adv. Sci.* **2020**, *7*, 1902988.
- [17] J. Xu, Y. He, S. Bi, M. Wang, P. Yang, D. Wu, J. Wang, F. Zhang, *Angew. Chem. Int. Ed.* **2019**, *58*, 12065-12069.
- [18] S. Bi, P. Thiruvengadam, S. Wei, W. Zhang, F. Zhang, L. Gao, J. Xu, D. Wu, J.-S. Chen, F. Zhang, *J. Am. Chem. Soc.* **2020**, *142*, 11893-11900.
- [19] S. Bi, C. Yang, W. Zhang, J. Xu, L. Liu, D. Wu, X. Wang, Y. Han, Q. Liang, F. Zhang, *Nat. Commun.* **2019**, *10*, 2467.
- [20] X. Li, J. Wang, F. Xue, Y. Wu, H. Xu, T. Yi, Q. Li, *Angew. Chem. Int. Ed.* **2021**, *60*, 2534-2540.
- [21] a) X. Wang, X. Ding, Y. Jin, D. Qi, H. Wang, Y. Han, T. Wang, J. Jiang, *Angew. Chem. Int. Ed.* **2023**, *62*, e202302808; b) N. Li, K. Jiang, F. Rodríguez-Hernández, H. Mao, S. Han, X. Fu, J. Zhang, C. Yang, C. Ke, X. Zhuang, *Adv. Sci.* **2022**, *9*, 2104898.
- [22] Y.-X. Ye, J. Pan, F. Xie, L. Gong, S. Huang, Z. Ke, F. Zhu, J. Xu, G. Ouyang, *P. Natl. Acad. Sci.* **2021**, *118*, e2103964118.
- [23] a) N. Li, J.-J. Liu, J.-W. Sun, B.-X. Dong, L.-Z. Dong, S.-J. Yao, Z. Xin, S.-L. Li, Y.-Q. Lan, *Green Chem.* **2020**, *22*, 5325-5332; b) J.-J. Liu, N. Li, J.-W. Sun, J. Liu, L.-Z. Dong, S.-J. Yao, L. Zhang, Z.-F. Xin, J.-W. Shi, J.-X. Wang, S.-L. Li, Y.-Q. Lan, *ACS Catal.* **2021**, *11*, 4510-4519.

## RESEARCH ARTICLE

- [24] a) J.-D. Yi, R. Xie, Z.-L. Xie, G.-L. Chai, T.-F. Liu, R.-P. Chen, Y.-B. Huang, R. Cao, *Angew. Chem. Int. Ed.* **2020**, *59*, 23641-23648; b) L. Wang, E. Guan, Y. Wang, L. Wang, Z. Gong, Y. Cui, X. Meng, B. C. Gates, F.-S. Xiao, *Nat. Commun.* **2020**, *11*, 1033.
- [25] W. Xie, H. Li, G. Cui, J. Li, Y. Song, S. Li, X. Zhang, J. Y. Lee, M. Shao, M. Wei, *Angew. Chem. Int. Ed.* **2021**, *60*, 7382-7388.
- [26] K. Lei, D. Wang, L. Ye, M. Kou, Y. Deng, Z. Ma, L. Wang, Y. Kong, *ChemSusChem* **2020**, *13*, 1725-1729.
- [27] L.-Z. Dong, L. Zhang, J. Liu, Q. Huang, M. Lu, W.-X. Ji, Y.-Q. Lan, *Angew. Chem. Int. Ed.* **2020**, *59*, 2659-2663.
- [28] a) J. Low, B. Dai, T. Tong, C. Jiang, J. Yu, *Adv. Mater.* **2019**, *31*, 1802981; b) Y.-J. Chen, Y.-Y. Wen, W.-H. Li, Z.-H. Fu, G.-E. Wang, G. Xu, *Nano Lett.* **2023**, *23*, 3614-3622.

## RESEARCH ARTICLE

## Entry for the Table of Contents



We developed a strategy for the evaluation of local electron density by controlling the relative electron-deficient property and electron-rich property of monomers based on three covalent organic frameworks. And, the VL-MCOF-1 exhibited excellent activities for CO<sub>2</sub> photoreduction, higher than VL-MCOF-2 and g-C<sub>34</sub>N<sub>6</sub>-COF, which is due to the synergistic effect of the electron-deficient unit, electron-rich unit, and efficient charge transfer channel.

The following is a personal Twitter handle for social media promotion:

Twitter handle: @langmuir\_mi

Twitter name: Meng